Journal of Applied Physics

RESEARCH ARTICLE | OCTOBER 01 2024

Near infrared to vacuum ultraviolet optical properties of $GdScO_3$

Prabin Dulal ; Emily Amonette ; Dylan Sotir ; Matthew R. Barone; Balaji Ramanujam; Ambalanath Shan ; Darrell G. Schlom ; Nikolas J. Podraza

J. Appl. Phys. 136, 135301 (2024)
https://doi.org/10.1063/5.0224848

Journal of Applied Physics ARTICLE pubs.aip.org/aip/jap

Near infrared to vacuum ultraviolet optical properties of $GdScO_3$

Cite as: J. Appl. Phys. **136**, 135301 (2024); doi: 10.1063/5.0224848
Submitted: 21 June 2024 · Accepted: 9 September 2024 ·
Published Online: 1 October 2024

View Online Export Citation CrossMark

Prabin Dulal,[1,a)] Emily Amonette,[1] Dylan Sotir,[2] Matthew R. Barone,[2] Balaji Ramanujam,[1] Ambalanath Shan,[1] Darrell G. Schlom,[2] and Nikolas J. Podraza[1,a)]

AFFILIATIONS

[1]Department of Physics and Astronomy and Wright Center for Photovoltaics Innovation and Commercialization, University of Toledo, Toledo, Ohio 43606, USA
[2]Department of Material Science and Engineering, Cornell University, Ithaca, New York 14583, USA

[a)]**Authors to whom correspondence should be addressed:** Prabin.Dulal@rockets.utoledo.edu and nikolas.podraza@utoledo.edu

ABSTRACT

Generalized ellipsometry measurements are used to extract the complex dielectric function ($\varepsilon = \varepsilon_1 + i\varepsilon_2$) spectra of $GdScO_3$ single crystals over the 0.7–8.5 eV photon energy range. $GdScO_3$ is a wide bandgap semiconductor with a high dielectric constant, and potential applications include replacing SiO_2 in silicon-based transistors and as an epitaxial substrate for thin film growth. This work presents the anisotropic optical properties for electric fields oscillating parallel to the *a*-, *b*-, and *c*-crystallographic axes. A direct bandgap is identified at 6.44 eV along the direction parallel to the *a*-axis, with additional critical points observed at 6.74 and 7.42 eV in the same direction. Additional above gap critical point transitions are found at 6.72, 7.31, and 7.96 along the direction parallel to the *b*-axis and 6.83 and 8.00 eV along the direction parallel to the *c*-axis.

INTRODUCTION

Gadolinium scandate ($GdScO_3$) has an orthorhombic perovskite crystal structure and belongs to the space group *Pbnm*.[1] The lattice parameters of $GdScO_3$ are $a = 5.45$, $b = 5.75$, and $c = 7.93$ Å.[2] The high dielectric constant, large bandgap energy, and thermal stability of $GdScO_3$ make it suitable as an alternative gate dielectric for future metal oxide semiconductor field effect transistors (MOSFETs) on silicon and has been proposed as a replacement candidate for SiO_2 in silicon-based transistors.[3,4] $GdScO_3$ also has potential for applications such as magnetic random-access memory (MRAM)[5] and has been explored for electronic applications.[6]

The material is anisotropic and exhibits different optical responses for electric fields oscillating parallel to each of the three orthogonal crystallographic axes. Two $GdScO_3$ single crystals with different Miller index surface planes, (001) and (110), are measured using generalized spectroscopic ellipsometry to obtain the anisotropic complex dielectric function tensor and optical response for electric fields oscillating parallel to each crystallographic axis. Measurements of $GdScO_3$ single crystals with (001) and (110) surface planes provide sensitivity to the optical properties of electric fields oscillating parallel to the three *a*-, *b*-, and *c*-crystallographic axes, respectively. The electric field components of incident light oscillate parallel and perpendicular to the plane of incidence. For the (001) crystal, the *c*-axis lies within the plane of incidence and is normal to the crystal surface, enabling the greatest sensitivity to the optical response parallel to the *a*- and *b*-axes that lie in the surface plane. For the (110) crystal, the electric components provide sensitivity to the optical response parallel to the *c*-axis in the surface plane. Perpendicular to the *c*-axis, the electric field oscillates along a convolution of the *a*- and *b*-axes. Rotation of the (001) crystal cut along different azimuthal angles provides sensitivity of the optical response along *a*- and *b*-axes since the axes lie in the sample plane. Rotation of the (110) crystal cut provides sensitivity of the optical response along the *c*-axis and perpendicular to the *c*-axis. Therefore, spectra collected at different azimuthal angle rotations of both $GdScO_3$ single crystals are fit simultaneously using a divided spectral range analysis approach to determine the complex dielectric function in each of the three crystallographic directions. In this work, the near infrared to vacuum ultraviolet anisotropic complex

optical properties are obtained using generalized ellipsometry over a photon range from 0.7 to 8.5 eV. The direct bandgap is identified at 6.44 eV and above bandgap critical points are found at 6.72, 6.74, 6.83, 7.31, 7.42, 7.96, and 8.00 eV.

EXPERIMENTAL METHODS

Czochralski grown 10 mm × 10 mm × 0.5 mm single-side polished (001) oriented, 5 mm × 5 mm × 0.5 mm single-side polished (110) oriented, and $10 \times 10 \times 0.5\ mm^3$ double-side polished (110) oriented $GdScO_3$ single crystals are obtained from MTI Corporation. A vacuum ultraviolet ellipsometer[7,8] (model VUV-VASE, J. A. Woollam) is used to measure the generalized ellipsometric spectra of single-side polished (110) and (001) oriented single crystals from 0.7 to 8.5 eV at an angle of incidence of 70°. The spectra between 3.0 and 4.0 eV exhibit substantial noise due to low sample reflectance and have been removed. Optical response varies with the crystal orientation as $GdScO_3$ is anisotropic in nature. The generalized ellipsometry measurements of (001) and (110) oriented crystals are collected with each sample being rotated manually about the respective surface normal to vary the azimuthal Euler angle three times, resulting in six sets of generalized ellipsometric spectra for analysis. The polar Euler angle remains 90° for any rotation of the (110) oriented crystal and 0° for the (001) oriented crystal. Measurements of the (001) oriented crystal are primarily sensitive to differences in electric field oscillations parallel to the *a*- and *b*-axes as those crystal axes are within the surface plane and yield different complex optical responses along those directions. The *a*- and *b*-axes directions are confirmed by x-ray diffraction (XRD). Rocking curves from the XRD (Empyrean, Malvern Panalytical Ltd.) of (110) and (001) surface cut single crystals reveal single peaks with nearly perfect symmetry and full width at half maximum (FWHM) of 0.004° and 0.015°, respectively, as shown in Fig. S10 in the supplementary material. The FWHM are small which indicates good crystalline quality.[9] For the (110) oriented crystal, measurements are primarily sensitive to the electric field parallel to the *c*-axis, which is parallel to the surface plane, and a convolution of the optical responses of the *a*- and *b*-axes which are at ∼47° and 43° with respect to the surface plane, respectively.

For each sample, a structural model consisting of semi-infinite $GdScO_3$ substrate with a surface layer is used to fit experimental generalized ellipsometric spectra. A least squares regression analysis minimizes the unweighted error function (σ).[10] The unweighted error function for generalized ellipsometric spectra ($N_{xy} = \cos 2\psi_{xy}$, $C_{xy} = \sin 2\psi_{xy} \cos\Delta_{xy}$, and $S_{xy} = \sin 2\psi_{xy} \sin\Delta_{xy}$) is defined as

$$\sigma = \left\{ \frac{1}{9n-m} \sum_{i=1}^{n} \left[\left(N_{pp,i}^{\mathrm{mod}} - N_{pp,i}^{\mathrm{exp}}\right)^2 + \left(C_{pp,i}^{\mathrm{mod}} - C_{pp,i}^{\mathrm{exp}}\right)^2 + \left(S_{pp,i}^{\mathrm{mod}} - S_{pp,i}^{\mathrm{exp}}\right)^2 + \left(N_{ps,i}^{\mathrm{mod}} - N_{ps,i}^{\mathrm{exp}}\right)^2 + \left(C_{ps,i}^{\mathrm{mod}} - C_{ps,i}^{\mathrm{exp}}\right)^2 + \left(S_{ps,i}^{\mathrm{mod}} - S_{ps,i}^{\mathrm{exp}}\right)^2 + \left(N_{sp,i}^{\mathrm{mod}} - N_{sp,i}^{\mathrm{exp}}\right)^2 + \left(C_{sp,i}^{\mathrm{mod}} - C_{sp,i}^{\mathrm{exp}}\right)^2 + \left(S_{sp,i}^{\mathrm{mod}} - S_{sp,i}^{\mathrm{exp}}\right)^2 \right] \right\}^{1/2}, \quad (1)$$

where n is the number of measured data points and m is the number of variable model parameters. The superscripts "exp" and "mod" refer to experimentally measured and model-simulated data. The subscripts *pp*, *ps*, and *sp* refer to N_{xy}, C_{xy}, and S_{xy} corresponding to $\rho_{pp} = \bar{r}_{pp}/\bar{r}_{ss} = \tan\psi_{pp} e^{i\Delta_{pp}}$, $\rho_{ps} = \bar{r}_{ps}/\bar{r}_{pp} = \tan\psi_{ps} e^{i\Delta_{ps}}$, and $\rho_{sp} = \bar{r}_{sp}/\bar{r}_{ss} = \tan\psi_{sp} e^{i\Delta_{sp}}$, where $\bar{r}_{xy}$ is the complex reflection ratio for incoming polarized light along the x direction (s or p) and reflected polarized light along the y direction (s or p).[11,12] ψ_{xy} and Δ_{xy} refer to the change in the amplitude and phase shift when light along the x direction (s or p) converts to the y direction (s or p).

Spectra in ε and structural parameters, including surface layer thickness and azimuthal Euler angles, are determined from the measured ellipsometric spectra using divided spectral range analysis.[13–17] In this approach, the full measured spectral range is divided into nominally transparent, weakly absorbing, and highly absorbing regions. A common structural model is used to describe the transparent and the highly absorbing spectral regions, while separate physically realistic optical models are applied to describe the spectra of ε in each direction within these spectral regions. No initial assumption is made for the behavior of ε in the weakly absorbing region, and it is excluded from the divided range analysis parametric fit. This method has been applied to obtain a physically realistic parametric model in the nominally transparent and highly absorbing spectral ranges. The transparent region extends from 0.7 to 5.0 eV and spectra in ε in each direction are described by using a constant additive term to ε_1 (ε_∞) and a Sellmeier expression,[18]

$$\varepsilon(E) = \varepsilon_\infty + \frac{2}{\pi}\left(\frac{AE_0}{E_0^2 - E^2}\right), \quad (2)$$

where A is the amplitude and E_0 is the resonance energy.

The highly absorbing spectral range is above the bandgap energy and extends from 7.0 to 8.5 eV. Spectra in ε are parameterized using ε_∞ and a sum of critical point parabolic band (CPPB) oscillators[19] along the direction parallel to *a*-, *b*-, and *c*-axes, and each CPPB oscillator is described by

$$\varepsilon = A_n e^{i\varphi_n}\left(\frac{\Gamma_n}{2E_n - 2E - i\Gamma_n}\right)^{\mu_n}, \quad (3)$$

where A_n is the amplitude, E_n is the critical point resonance energy, Γ_n is critical point broadening, φ_n is the phase projection factor, and μ_n is the dimensionality of the critical point. The exponent μ_n can have values of 1, 1/2, 0 (logarithmic), and −1/2 for excitonic, one, two, and three-dimensional critical points,

respectively. For the weakly absorbing region (5.0–7.0 eV), no line shape is assumed to describe ε so as not to impose a particular parametric model bias in the vicinity of the bandgap. In this analysis, the structural parameters are common for the transparent and heavily absorbing spectral ranges, which are simultaneously fit. A unique azimuth Euler angle (ϕ) for each sample rotation measurement of each crystal and a common surface layer thickness is obtained for each crystal cut sample.

The structural model consists of semi-infinite $GdScO_3$ and a surface layer. The surface layer is represented as an anisotropic layer with the same Euler angles as in the bulk crystal and unique optical response in each principal direction. The optical response of the surface layer in each principal direction is described by a Bruggeman effective medium approximation (EMA)[20,21] consisting of equal parts of the optical response along the respective crystallographic axis and void defined as

$$\left(\frac{\varepsilon_{mat}-\varepsilon}{\varepsilon_{mat}+2\varepsilon}\right)(1-f_{void})+\left(\frac{\varepsilon_{void}-\varepsilon}{\varepsilon_{void}+2\varepsilon}\right)f_{void}=0, \quad (4)$$

where f_{void} is the void volume fraction. The surface layers are determined to be 5.9 ± 0.6 and 6.2 ± 0.6 nm thick for the (001) and (110) oriented crystals, respectively. Atomic force microscopy (AFM) (Veeco D3100, Veeco Instruments Inc.) shows root mean square roughness thicknesses of 3.23 and 0.86 nm for (110) and (001) oriented samples, respectively, as shown in Fig. S9 in the supplementary material. The differences in the AFM surface roughness thicknesses and surface layer thicknesses from spectroscopic ellipsometry are attributed to different methods of extraction. AFM profiles the surface of the sample to give information about surface topography, and it may not be definitive since it is only sensitive to local surface roughness that does not include information on density of the layer and may not be able to detect the deepest voids in the surface layer over the area of the measurement.[21–23] However, the Bruggeman effective medium approximation used in spectroscopic ellipsometry data analysis treats the surface layer as a discrete layer with different optical response than the bulk which has different surface effects and density.[21] As such, the spectroscopic ellipsometry determined surface layer thickness may include contributions from roughness sampled over the ~1 mm diameter of the beam spot, a lower density sub-surface layer, different bonding configurations and composition of the surface, and any chemical species absorbed on the surface.

Structural parameters obtained from divided range analysis are used as fixed parameters when extracting ε. Numerical inversion[24] is used to fit all three sets of generalized ellipsometric spectra at three azimuthal angles collected for each of the (001) and (110) oriented crystal cuts simultaneously, including the initially ignored weakly absorbing region to extract ε along the three crystallographic axes.

RESULTS AND DISCUSSION

Figures S1 and S2 in the supplementary material show experimental ellipsometric spectra fit from 0.7 to 8.5 eV using divided spectral range analysis for the (001) and (110) oriented single crystals of $GdScO_3$ at different azimuthal angles. After fixing the structural parameters obtained from divided spectral range analysis, numerical inversion is used to extract ε parallel to each principal direction over the entire measured spectral range with the results shown in Fig. S5 in the supplementary material. The resultant quality of fit, σ, obtained is 9.1×10^{-2}. The relatively high σ is due to simultaneously fitting all directions to obtain the optical response along the *a*-, *b*-, and *c*-axes. All parameter values obtained are physically realistic and with low error.

Critical point transitions in ε corresponding to each direction are identified by simultaneously fitting each numerically inverted spectrum in ε_2 and the corresponding first order derivative $d\varepsilon_2/dE$ using a sum of CPPB oscillators. Sub-gap absorption is not considered at this point, so the lower photon energy limit is chosen to be the photon energy where $\varepsilon_2 > 0.5$ in each direction, and the upper photon energy limit is 8.5 eV. All combinations of critical point dimensionalities are evaluated, and the combination with the highest quality of fit reflected in the lowest mean square error between the CPPB model and numerically inverted spectra is identified along with the critical point transition parameters for each CPPB oscillator. Results of these fits are shown in Fig. 1 and critical point transition parameters reported in Tables I–III.

The CPPB model is not applicable to define spectra in ε within the weakly absorbing and transparent spectral ranges in the vicinity of the bandgap and below it. Therefore, a piecewise parameterization is developed that includes an Urbach tail below the bandgap energy to account for sub-gap absorption and CPPB behavior at and above the bandgap energy.[25,26] The modified imaginary part of CPPB-based parameterization of ε is given as

$$\varepsilon_2 = \begin{cases} \frac{E_0}{E}\exp\left[\frac{E-E_t}{E_U}\right], & 0 < E \le E_t, \\ Im\sum[\varepsilon_{CPPB}(E)], & E > E_t, \end{cases} \quad (5)$$

where $E_t = E_0 + 0.5\,E_U$ for a direct transition. E_0 is the lowest energy critical point transition, and E_U represents the width of the Urbach tail. The numerically inverted ε_2 spectrum parallel to the *a*-axis contains the lowest energy direct transition of any direction. This lowest energy transition is the direct bandgap for $GdScO_3$, with any absorption below this transition represented by the Urbach tail. The Urbach energy is a fit parameter and has a value of 42 ± 31 meV. Kramers–Kronig integration of corresponding spectra in ε_2 is used to describe ε_1,

$$\varepsilon_1 = \varepsilon_\infty + \frac{2}{\pi}\left(\frac{AE_0}{E_0^2 - E^2}\right) + \frac{2}{\pi}P\int_{0.7}^{8.5}\frac{\xi\varepsilon_2(\xi)}{\xi^2 - E^2}d\xi, \quad (6)$$

where P is Cauchy's principal part of the Kramers–Kronig integral and ε_∞ is fixed to 1 along with the inclusion of a Sellmeier expression.

For spectra in ε_2 parallel to the *b*- and *c*-axes, reduced transition strengths above the direct bandgap energy identified from spectra in ε_2 parallel to the *a*-axis are modeled using a Cody band edge function to modify the CPPB parametric

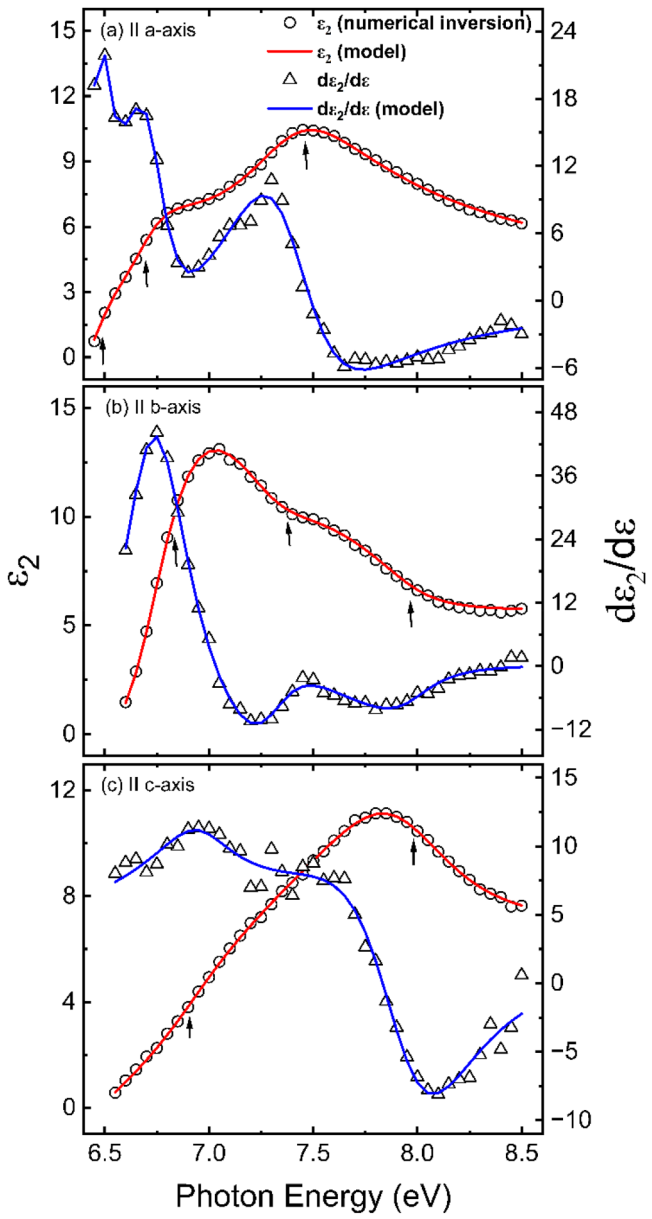

FIG. 1. Spectra in ε_2 of $GdScO_3$ obtained from numerical inversion (open circles) and its first derivative (open triangles) with respect to photon energy and simultaneous parametric fits (red lines and blue lines) using CPPB oscillators in directions parallel to the (a) *a*-axis (b) *b*-axis, and (c) *c*-axis. Arrows indicate the positions of critical points.

model defined as

$$\varepsilon_2 = \begin{cases} 0, & 0 < E \le E_g, \\ G_c(E) \sum Im[\varepsilon_{\mathrm{CPPB}}(E)], & E > E_g, \end{cases} \tag{7}$$

TABLE I. CPPB oscillator parameters describing numerically inverted spectra in ε_2 and its derivative simultaneously along the direction parallel to the *a*-axis for $GdScO_3$. ε_∞ is fixed at 1 with a Sellmeier amplitude and energy at 27.2 ± 0.8 and 10.6 ± 0.1 eV, respectively. The resultant σ is 5.3×10^{-4}.

Parameter, critical point (n)	0	1	2
E_n (eV)	6.44 ± 0.03	6.74 ± 0.02	7.42 ± 0.02
A_n	3.4 ± 0.5	3.7 ± 0.6	9.8 ± 0.5
Γ_n (eV)	0.2 ± 0.1	0.31 ± 0.04	0.72 ± 0.03
ϕ_n (°)	−110 ± 59	−0.16 ± 19.32	23 ± 4
μ_n	0.5	0.5	0.5

where G_c is the Cody band edge function,[18]

$$G_c(E) = \frac{(E - E_g)^2}{(E - E_g)^2 + E_p^2}, \tag{8}$$

where E_p defines a transition energy, $E_g - E_0$. Above this energy, higher energy critical point behavior in the form of the CPPB oscillator is reflected in ε_2 such that $G_c(E) \to 1$ when $E \gg E_p + E_g$. In the vicinity of the bandgap, $G_c(E) \to 0$ when $E - E_g \to 0$. E_g is fixed at the lowest energy critical point obtained along the direction parallel to the *a*-axis such that E_g marks the absorption onset for the *b*- and *c*-directions. Absorption at photon energies below the lowest critical point in the optical response for electric fields oscillating parallel to the *b*- and *c*-directions is attributed to indirect transitions in the $GdScO_3$ crystals.[27] This absorption below the observed lowest energy critical point transition in each direction is attributed to reduced transition strengths along that direction and is accounted for by the Cody band edge function. For the final parameterization of ε parallel to the *b*- and *c*-axes, all other parameters except the amplitude and phase of the critical points are fixed to the values obtained by fitting numerically inverted ε_2 and its derivative simultaneously using the CPPB model. Hence, amplitude and the phase are the only variable fit parameters needed to describe ε_2 along with the Cody band edge function for electric fields oscillating parallel to the *b*- and *c*-axes. The real part of the complex dielectric function ε_1 is obtained from Kramers–Kronig integration of ε_2, a Sellmeier expression, and ε_∞. Figures S3 and S4 in the supplementary material show experimental generalized ellipsometric spectra fit from 0.7 to 8.5 eV using the full

TABLE II. CPPB oscillator parameters describing numerically inverted spectra in ε_2 and its derivative simultaneously along the direction parallel to the *b*-axis for $GdScO_3$. The resultant σ is 6.6×10^{-4}.

Parameter, critical point (n)	0	1	2
E_n (eV)	6.72 ± 0.01	7.31 ± 0.03	7.96 ± 0.03
A_n	26 ± 2	5 ± 2	5 ± 2
Γ_n (eV)	0.51 ± 0.03	0.49 ± 0.10	0.38 ± 0.08
ϕ_n (°)	−56 ± 5	210 ± 15	100 ± 3
μ_n	0.5	0.5	−0.5

TABLE III. CPPB oscillator parameters describing numerically inverted spectra in ε_2 and its derivative simultaneously along the direction parallel to the *c*-axis for $GdScO_3$. The resultant σ is 7.3×10^{-4}.

Parameter, critical point (n)	0	1
E_n (eV)	6.83 ± 0.03	8.00 ± 0.04
A_n	4 ± 1	6.3 ± 0.3
Γ_n (eV)	0.5 ± 0.1	0.99 ± 0.05
ϕ_n (°)	−145 ± 4	60 ± 9
μ_n	−0.5	1

parametric models describing spectra in ε over that range for the (001) and (110) oriented $GdScO_3$ single crystals. Figure S6 in the supplementary material shows the resulting numerically inverted and parametric model fit of spectra in ε for each principal direction of $GdScO_3$.

The response of electric field components oscillating parallel to each of the crystallographic directions in an orthorhombic crystal may exhibit strong differences.[28–30] Therefore, different models have been used along the three orthogonal directions to account for the different responses of electric field components in each of the three crystallographic directions. CPPB oscillators alone do not describe the absorption below the lowest direct transition. Hence, to account for the absorption below the lowest direct transition, the CPPB model is modified with an Urbach tail or a Cody function. Along the direction parallel to the *a*-axis, there is absorption below the lowest direct transition at 6.44 eV, which is the lowest direct transition among all three crystallographic directions. Therefore, the CPPB-based model is combined with an Urbach tail to account for absorption below the lowest critical point transition. However, the lowest direct transitions are at 6.72 and 6.83 eV along the direction parallel to the *b*- and *c*-axes, respectively, which are at higher photon energies than the lowest critical point energy at 6.44 eV for electric fields oscillating along the *a*-axis. For electric fields oscillating parallel to the *b*- and *c*-axes, the CPPB model is modified with a Cody function to account for the reduced transition strength of any optical transition between their respective lowest critical points and the overall critical point energy at 6.44 eV along the *a*-axis.

The resulting numerically inverted, divided spectral range analysis, and parametric model fit spectra in ε of $GdScO_3$ along each direction are shown in Fig. 2, and parameters along the *b*- and *c*-axes are listed in Tables IV and V. The lowest energy critical point describing the direct bandgap in any direction is identified in the optical response parallel to the *a*-axis and is found to be 6.44 ± 0.02 eV, while two other higher energy critical point transitions in this direction are identified at 6.74 and 7.42 eV. Three critical points are identified in the optical response parallel to the *b*-axis at 6.72, 7.31, and 7.96 eV, yielding $E_p = 0.28$ eV. Similarly, the two critical points identified in the optical response parallel to the *c*-axis are at 6.83 and 8.00 eV with $E_p = 0.39$ eV. The critical point transitions identified at 6.72 eV along the direction parallel to the *b*-axis and 6.74 eV along the *a*-axis are within the error of each other, indicating that these may be the same features. All critical points have phases as non-integer multiples of π/2, meaning they

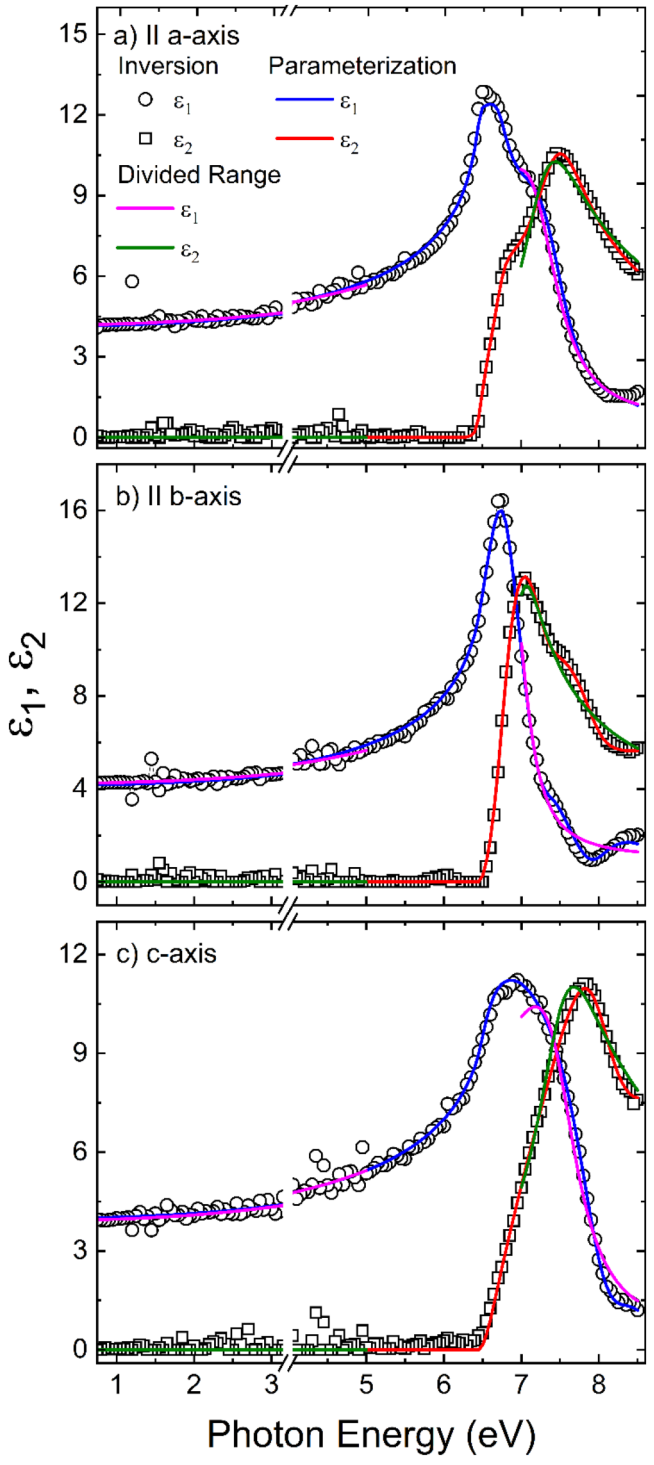

FIG. 2. $GdScO_3$ spectra in ε obtained from numerical inversion (open symbols), full spectral range parameterization (lines), and divided spectral range parametric fit (lines) along directions parallel to the (a) *a*-axis, (b) *b*-axis, and (c) *c*-axis.

TABLE IV. CPPB oscillators with Cody band edge parameters describing numerically inverted spectra in ε_2 along the direction parallel to the *b*-axis. Parameters not described are fixed to values obtained by CPPB fitting only (Table II). ε_∞ is fixed at 1, with a Sellmeier amplitude and energy at 26.4 ± 0.9 and 10.7 ± 0.2 eV, respectively.

A_0	46 ± 2
ϕ_0 (°)	312 ± 3
A_1	15 ± 1
ϕ_1 (°)	207 ± 3
A_2	73 ± 8
ϕ_2 (°)	99 ± 2
E_g (eV)	6.44

are caused by discrete excitations with a continuous background and excitonic effects.[31] Optical gaps are identified for electric fields oscillating parallel to each of the three crystallographic directions, and the lowest direct transition is found along the direction parallel to the *a*-axis which is identified as the bandgap of $GdScO_3$. The effective birefringence and dichroism between the given directions are shown in Fig. 3.

Additionally, as shown in Fig. S7 in the supplementary material, unpolarized and polarized transmission measurements of a double-side polished 0.5 mm thick (110) surface plane cut single crystal $GdScO_3$ have been made over a spectral range of 0.7–6.4 eV (model V-VASE, J.A. Woollam). Polarized transmission measurements are made such that the electric fields oscillate parallel and perpendicular to the *c*-axis in the (110) cut crystal surface plane. Transmission spectra shows the sub-bandgap features which are attributed to the crystal symmetry split features of transition metal d-states.[32] The average absorption coefficient ($\alpha = 4\pi k/\lambda$) of the (110) oriented $GdScO_3$ single crystal is shown in Fig. S8 in the supplementary material, which shows the unpolarized results are intermediate to those with electric fields polarized perpendicular and parallel to the *c*-axis. A transfer matrix based method has been used to first extract an average extinction coefficient (k) from transmittance spectra via numerical inversion assuming an index of refraction (n) as the weighted average of n from ellipsometry along the three crystallographic directions based on the projection of each crystal axis into the (110) surface plane, a surface layer thickness of 6.2 nm from ellipsometry of the single-side polished (110) crystal, and 0.53 mm thickness of the double-side polished (110) crystal. The crystal is opaque at photon energies >6.1 eV, prohibiting reliable

TABLE V. CPPB oscillators with Cody band edge parameters describing numerically inverted spectra in ε_2 along the direction parallel to the *c*-axis. Parameters not described are fixed to values obtained by CPPB fitting only (Table III). ε_∞ is fixed at 1 with a Sellmeier amplitude and energy at 26 ± 1 and 10.9 ± 0.2 eV, respectively.

A_0	33 ± 1
ϕ_0 (°)	144 ± 5
A_1	6.4 ± 0.2
ϕ_1 (°)	62 ± 3
E_g (eV)	6.44

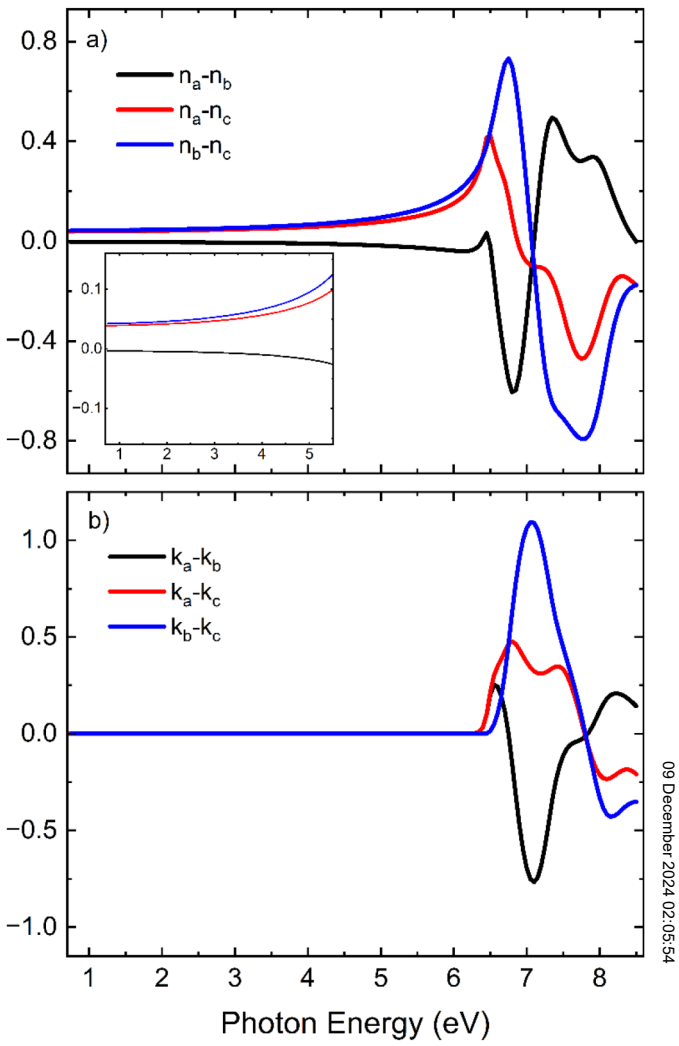

FIG. 3. (a) Birefringence (top) and (b) dichroism (bottom) based on the complex optical property differences for the three optically distinct crystallographic directions of $GdScO_3$.

values of absorption coefficient to be obtained at high photon energies. The low values of absorption coefficient (<200 cm^{-1}) obtained from transmittance up to 6.1 eV are not likely associated with band-to-band transitions as absorption coefficient values associated with direct transitions are ~10^4 cm^{-1}.[33,34] High absorption coefficient values obtained from ellipsometry as shown in Fig. S8 in the supplementary material are from band-to-band transitions and indicate a direct gap at 6.44 eV. As transmittance-based absorption coefficient spectra from 6.1 to 6.44 eV are not obtainable at present, the current transmittance results indicate that a bandgap is no smaller than 6.1 eV for single crystal $GdScO_3$.

Different techniques have been used to determine the bandgap of $GdScO_3$ as reported in Table VI. Schafer *et al.* report

TABLE VI. Reported bandgap energies of $GdScO_3$.

	Bandgap energy	Methods
Raekers *et al.*[35]	5.8 eV	XAS, x-ray photoelectron spectroscopy, x-ray emission spectroscopy
Cicerrella[38]	5.2 eV	Spectroscopic ellipsometry
Lim *et al.*[32]	6.5 eV	Spectroscopic ellipsometry
Lucovksy *et al.*[40]	5.8 eV	XAS
Schafer *et al.*[37]	5.2 and 4.6 eV	X-ray photoelectron spectroscopy and DFT calculation
Mizzi *et al.*[36]	5.2 eV	X-ray photoelectron spectroscopy, UV photoelectron spectroscopy, and DFT
This work	6.45 eV	Spectroscopic ellipsometry

the bandgap of orthorhombic $GdScO_3$ using x-ray photoluminescence spectroscopy and density functional theory (DFT) calculations as 5.2 and 4.65 eV, respectively.[37] Lim *et al.* report the bandgap of single crystal $GdScO_3$ by spectroscopic ellipsometry to be 6.5 eV.[32] Cicerrella also studied $GdScO_3$ films deposited on $LaAlO_3$ by spectroscopic ellipsometry and found the bandgap at 6.12 eV.[38] Derks *et al.* report the bandgap of Czochralski grown single crystal $GdScO_3$ by x-ray absorption spectroscopy and x-ray emission spectroscopy as 5.8 eV.[39] Lucovsky *et al.* also characterized single crystal $GdScO_3$ using x-ray absorption spectroscopy (XAS) and found the bandgap at 5.8 eV.[40] These differences in the bandgap energy are attributed to different methods of characterization and extraction of the bandgap value. Moreover, some of these differences are also accounted for by strain associated with epitaxial film grown on the substrate. The bandgap of $GdScO_3$ single crystal obtained is in close agreement with that obtained through spectroscopic ellipsometry by Lim *et al.*[32] A slight difference in the bandgap energy obtained by spectroscopic ellipsometry of the epitaxial film may be due to the lattice mismatch between $GdScO_3$ and the substrate, which introduces strain in the epitaxial $GdScO_3$ film compared to that of single crystal $GdScO_3$,[41,42] or due to film deposition conditions and different modeling approaches.

CONCLUSION

Measurements of $GdScO_3$ single crystals with (001) and (110) Miller index surface planes provide sensitivity to the optical properties for electric fields oscillating parallel to the *a*-, *b*-, and *c*-crystallographic axes. The anisotropic optical properties of $GdScO_3$ single crystal have been determined over the spectral range from 0.7 to 8.5 eV. The lowest direct transition has been observed at 6.44 eV and is considered the direct bandgap energy. Critical point transitions along the *a*-, *b*-, and *c*-axes have been identified within the measured spectral range. Additional above gap critical point transitions along the *a*-, *b*-, and *c*-axes have been identified at 6.72, 6.74, 6.83, 7.31, 7.42, 7.96, and 8.00 eV.

SUPPLEMENTARY MATERIAL

See the supplementary material for detailed information of generalized ellipsometric spectra of $GdScO_3$ and parameterized model fit, table of fit parameters, x-ray diffraction, and AFM results.

ACKNOWLEDGMENTS

This material is based on research sponsored by the Air Force Research Laboratory under Agreement No. FA9453-21-C-0056. The U.S. Government is authorized to reproduce and distribute reprints for Governmental purposes notwithstanding any copyright notation thereon. The views expressed are those of the authors and do not reflect the official guidance or position of the United States Government, the Department of Defense, or the United States Air Force. The appearance of external hyperlinks does not constitute endorsement by the United States Department of Defense (DoD) of the linked websites, or the information, products, or services contained therein. The DoD does not exercise any editorial, security, or other control over the information you may find at these locations. Approved for public release; distribution is unlimited. Public Affairs release approval No. AFRL-2023-3863.

AUTHOR DECLARATIONS

Conflict of Interest

The authors have no conflicts to disclose.

Author Contributions

Prabin Dulal: Conceptualization (equal); Data curation (equal); Formal analysis (equal); Writing – original draft (equal); Writing – review & editing (equal). **Emily Amonette:** Data curation (supporting); Writing – review & editing (supporting). **Dylan Sotir:** Data curation (supporting). **Matthew R. Barone:** Data curation (supporting). **Balaji Ramanujam:** Data curation (supporting). **Ambalanath Shan:** Data curation (supporting). **Darrell G. Schlom:** Resources (supporting); Supervision (supporting). **Nikolas J. Podraza:** Conceptualization (equal); Funding acquisition (equal); Supervision (equal); Writing – review & editing (equal).

DATA AVAILABILITY

The data that support the findings of this study are available from the corresponding author upon reasonable request.

REFERENCES

[1]R. Uecker, H. Wilke, D. G. Schlom, B. Velickov, P. Reiche, A. Polity, M. Bernhagen, and M. Rossberg, "Spiral formation during Czochralski growth of rare-earth scandates," J. Cryst. Growth **295**(1), 84–91 (2006).
[2]J. Schubert, O. Trithaveesak, A. Petraru, C. L. Jia, R. Uecker, P. Reiche, and D. G. Schlom, "Structural and optical properties of epitaxial $BaTiO_3$ thin films grown on $GdScO_3$ (110)," Appl. Phys. Lett. **82**(20), 3460–3462 (2003).
[3]H. M. Christen, G. E. Jellison, Jr., I. Ohkubo, S. Huang, M. E. Reeves, E. Cicerrella, J. L. Freeouf, Y. Jia, and D. G. Schlom, "Dielectric and optical properties of epitaxial rare-earth scandate films and their crystallization behavior," Appl. Phys. Lett. **88**(26), 262906 (2006).

[4]T. Heeg, J. Schubert, C. Buchal, E. Cicerrella, J. L. Freeouf, W. Tian, Y. Jia, and D. G. Schlom, "Growth and properties of epitaxial rare-earth scandate thin films," Appl. Phys. A **83**(1), 103–106 (2006).
[5]M. Wagner, T. Heeg, J. Schubert, S. Lenk, S. Mantl, C. Zhao, M. Caymax, and S. De Gendt, "Gadolinium scandate thin films as an alternative gate dielectric prepared by electron beam evaporation," Appl. Phys. Lett. **88**(17), 172901 (2006).
[6]F. H. Gecit and S. Cabuk, "Structure and electronic properties of $LnScO_3$ compounds: A GGA+ U calculation," Comput. Mater. Sci. **208**, 111350 (2022).
[7]T. Wagner, J. N. Hilfiker, T. E. Tiwald, C. L. Bungay, and S. Zollner, "Materials characterization in the vacuum ultraviolet with variable angle spectroscopic ellipsometry," Phys. Status Solidi A **188**(4), 1553–1562 (2001).
[8]J. N. Hilfiker, C. L. Bungay, R. A. Synowicki, T. E. Tiwald, C. M. Herzinger, B. Johs, G. K. Pribil, and J. A. Woollam, "Progress in spectroscopic ellipsometry: Applications from vacuum ultraviolet to infrared," J. Vac. Sci. Technol. A **21**(4), 1103–1108 (2003).
[9]D. H. Jang, W.-J. Lee, E. Sohn, H. J. Kim, D. Seo, J.-Y. Park, E. J. Choi, and K. H. Kim, "Single crystal growth and optical properties of a transparent perovskite oxide $LaInO_3$," J. Appl. Phys. **121**(12), 125109 (2017).
[10]B. Johs and C. M. Herzinger, "Quantifying the accuracy of ellipsometer systems," Phys. Status Solidi C **5**(5), 1031–1035 (2008).
[11]G. E. Jellison, Jr., R. P. Hermann, E. D. Specht, L. A. Boatner, T. Zac Ward, and A. Herklotz, "Generalized ellipsometry measurements of crystalline thin film and bulk tin oxide," Phys. Status Solidi A **219**(16), 2100378 (2022).
[12]T. E. Tiwald and M. Schubert, "Measurement of rutile TiO_2 dielectric tensor from 0.148 to 33 μm using generalized ellipsometry," in *Optical Diagnostic Methods for Inorganic Materials II 4103* (SPIE, 2000), pp. 19–29.
[13]L. Karki Gautam, H. Haneef, M. M. Junda, D. B. Saint John, and N. J. Podraza, "Approach for extracting complex dielectric function spectra in weakly-absorbing regions," Thin Solid Films **571**, 548–553 (2014).
[14]F. V. Hensling, D. Dahliah, P. Dulal, P. Singleton, J. Sun, J. Schubert, H. Paik *et al.*, "Epitaxial stannate pyrochlore thin films: Limitations of cation stoichiometry and electron doping," APL Mater. **9**(5), 051113 (2021).
[15]B. Subedi, L. Guan, Y. Yu, K. Ghimire, P. Uprety, Y. Yan, and N. J. Podraza, "Formamidinium + cesium lead triiodide perovskites: Discrepancies between thin film optical absorption and solar cell efficiency," Sol. Energy Mater. Sol. Cells **188**, 228–233 (2018).
[16]D. Adhikari, M. M. Junda, P. Uprety, K. Ghimire, I. Subedi, and N. J. Podraza, "Near infrared to ultraviolet anisotropic optical properties of single crystal $SrLaAlO_4$ from spectroscopic ellipsometry," Phys. Status Solidi B **253**(10), 2066–2072 (2016).
[17]M. Barone, M. Foody, Y. Hu, J. Sun, B. Frye, S. S. Perera, B. Subedi *et al.*, "Growth of Ta_2SnO_6 films, a candidate wide-band-gap p-type oxide," J. Phys. Chem. C **126**(7), 3764–3775 (2022).
[18]R. W. Collins and A. S. Ferlauto, "Optical physics of materials," ChemInform **37**(11), 93–233 (2006).
[19]D. E. Aspnes, in *Handbook on Semiconductors*, edited by M. Balkanskki (North-Holland, Amsterdam, 1980), pp. 125–127.
[20]D. E. Aspnes, J. B. Theeten, and F. Hottier, "Investigation of effective-medium models of microscopic surface roughness by spectroscopic ellipsometry," Phys. Rev. B **20**(8), 3292–3302 (1979).
[21]H. Fujiwara, J. Koh, P. I. Rovira, and R. W. Collins, "Assessment of effective-medium theories in the analysis of nucleation and microscopic surface roughness evolution for semiconductor thin films," Phys. Rev. B **61**(16), 10832–10844 (2000).
[22]P. Petrik, L. P. Biró, M. Fried, T. Lohner, R. Berger, C. Schneider, J. Gyulai, and H. Ryssel, "Comparative study of surface roughness measured on polysilicon using spectroscopic ellipsometry and atomic force microscopy," Thin Solid Films **315**(1–2), 186–191 (1998).
[23]T. A. Mykhaylyk, N. L. Dmitruk, S. D. Evans, I. W. Hamley, and J. R. Henderson, "Comparative characterisation by atomic force microscopy and ellipsometry of soft and solid thin films," Surf. Interface Anal. **39**(7), 575–581 (2007).
[24]W. G. Oldham, "Numerical techniques for the analysis of lossy films," Surf. Sci. **16**, 97–103 (1969).
[25]I. Subedi, M. A. Slocum, D. V. Forbes, S. M. Hubbard, and N. J. Podraza, "Optical properties of InP from infrared to vacuum ultraviolet studied by spectroscopic ellipsometry," Appl. Surf. Sci. **421**, 813–818 (2017).
[26]M. M. Junda, C. R. Grice, I. Subedi, Y. Yan, and N. J. Podraza, "Effects of oxygen partial pressure, deposition temperature, and annealing on the optical response of CdS:O thin films as studied by spectroscopic ellipsometry," J. Appl. Phys. **120**(1), 015306–015308 (2016).
[27]G. Lucovsky, Y. Zhang, J. L. Whitten, D. G. Schlom, and J. L. Freeouf, "Separate and independent control of interfacial band alignments and dielectric constants in transition metal rare earth complex oxides," Microelectron. Eng. **72**(1–4), 288–293 (2004).
[28]E. Amonette, P. Dulal, D. Sotir, M. Barone, D. Schlom, and N. J. Podraza, "Band gap energy and near infrared to ultraviolet complex optical properties of single crystal $TbScO_3$," Appl. Phys. Lett. **123**(5), 052103 (2023).
[29]L. Velasco Davoise, R. Peña Capilla, and A. M. Díez-Pascual, "Isotropic and anisotropic complex refractive index of PEDOT: PSS," Polymers **15**(15), 3298 (2023).
[30]M. I. Alonso and M. Garriga, "Optical properties of anisotropic materials: An experimental approach," Thin Solid Films **455**, 124–131 (2004).
[31]P. Lautenschlager, M. Garriga, S. Logothetidis, and M. Cardona, "Interband critical points of GaAs and their temperature dependence," Phys. Rev. B **35**(17), 9174–9189 (1987).
[32]S.-G. Lim, S. Kriventsov, T. N. Jackson, J. H. Haeni, D. G. Schlom, A. M. Balbashov, R. Uecker, P. Reiche, J. L. Freeouf, and G. Lucovsky, "Dielectric functions and optical bandgaps of high-K dielectrics for metal-oxide-semiconductor field-effect transistors by far ultraviolet spectroscopic ellipsometry," J. Appl. Phys. **91**(7), 4500–4505 (2002).
[33]G. E. Jellison, Jr., I. Paulauskas, L. A. Boatner, and D. J. Singh, "Optical functions of $KTaO_3$ as determined by spectroscopic ellipsometry and comparison with band structure calculations," Phys. Rev. B **74**(15), 155130 (2006).
[34]J. I. Pankove, *Optical Processes in Semiconductors* (Courier Corporation, 1975).
[35]M. Raekers, K. Kuepper, S. Bartkowski, M. Prinz, A. V. Postnikov, K. Potzger, S. Zhou *et al.*, "Electronic and magnetic structure of R ScO_3 (R = Sm, Gd, Dy) from x-ray spectroscopies and first-principles calculations," Phys. Rev. B **79**(12), 125114 (2009).
[36]C. A. Mizzi, P. Koirala, and L. D. Marks, "Electronic structure of lanthanide scandates," Phys. Rev. Mater. **2**(2), 025001 (2018).
[37]A. Schäfer, K. Rahmanizadeh, G. Bihlmayer, M. Luysberg, F. Wendt, A. Besmehn, A. Fox *et al.*, "Polymorphous $GdScO_3$ as high permittivity dielectric," J. Alloys Compd. **651**, 514–520 (2015).
[38]E. Cicerrella, "Dielectric functions and optical bandgaps of high-K dielectrics by far ultraviolet spectroscopic ellipsometry," Ph.D. dissertation (Oregon Health and Science University, 2006).
[39]C. Derks, K. Kuepper, M. Raekers, A. V. Postnikov, R. Uecker, W. L. Yang, and M. Neumann, "Band-gap variation in R ScO_3 (R = Pr, Nd, Sm, Eu, Gd, Tb, and Dy): X-ray absorption and O K-edge x-ray emission spectroscopies," Phys. Rev. B **86**(15), 155124 (2012).
[40]G. Lucovsky, J. G. Hong, C. C. Fulton, Y. Zou, R. J. Nemanich, H. Ade, D. G. Scholm, and J. L. Freeouf, "Spectroscopic studies of metal high-k dielectrics: Transition metal oxides and silicates, and complex rare earth/transition metal oxides," Phys. Status Solidi B **241**(10), 2221–2235 (2004).
[41]Q. Yan, P. Rinke, A. Janotti, M. Scheffler, and C. G. Van de Walle, "Effects of strain on the band structure of group-III nitrides," Phys. Rev. B **90**(12), 125118 (2014).
[42]M. K. Mainali, I. Subedi, D. V. Forbes, S. M. Hubbard, and N. J. Podraza, "Optical and electronic transport properties of epitaxial InGaAs and InAlAs in multilayer stacks," J. Mater. Sci. **58**, 9533–9546 (2023).